Journal of Physics D: Applied Physics

Van der Waals heterostructures of MoS₂ and Janus MoSSe monolayers on graphitic boron-carbon-nitride (BC₃, C₃N, C₃N₄ and C₄N₃) nanosheets: a first-principles study

To cite this article before publication: Asdollah Baafekry *et al* 2020 *J. Phys. D: Appl. Phys.* in press https://doi.org/10.1088/1361-6463/ab876c

Van der Waals heterostructures of MoS_2 and Janus MoSSe monolayers on graphitic boron-carbon-nitride (BC_3, C_3N, C_3N_4 and C_4N_3) nanosheets: A First-Principles study

A. Bafekry,[1,2,*] M. Yagmurcukardes,[2] B. Akgenc,[3] M. Ghergherehchi,[4,†] and Ch. V. Nguyen[5]

[1] *Department of Physics, University of Guilan, 41335-1914 Rasht,Iran*
[2] *Department of Physics, University of Antwerp, Groenenborgerlaan 171, B-2020 Antwerp, Belgium*
[3] *Department of Physics, Kirklareli University, Kirklareli, 39100, Turkey*
[4] *College of Electronic and Electrical Engineering, Sungkyun kwan University, Suwon, Korea*
[5] *Department of Materials Science and Engineering, Le Quy Don Technical University, Hanoi, Vietnam*

(Dated: April 1, 2020)

In this work, we extensively investigate the structural and electronic properties of van der Waals heterostructures (HTs) constructed by MoS_2/BC_3, MoS_2/C_3N, MoS_2/C_3N_4, MoS_2/C_4N_3 and those using Janus MoSSe instead of MoS_2 by performing density functional theory calculations. The electronic band structure calculations and the corresponding partial density of states reveal that the significant changes are driven by quite strong layer-layer interaction between the constitutive layers. Our results show that although all monolayers are semiconductors as free-standing layers, the MoS_2/C_3N and MoS_2/C_4N_3 bilayer HTs display metallic behavior as a consequence of transfer of charge carriers between two constituent layers. In addition, it is found that in MoSSe/C_3N bilayer HT, the degree of metallicity is affected by the interface chalcogen atom type when Se atoms are facing to C_3N layer, the overlap of the bands around the Fermi level is smaller. Moreover, the half-metallic magnetic C_4N_3 is shown to form magnetic half-metallic trilayer HT with MoS_2 independent of the stacking sequence, i.e. whether it is sandwiched or two C_4N_3 layer encapsulate MoS_2 layer. We further analyze the trilayer HTs in which MoS_2 is encapsulated by two different monolayers and it is revealed that at least with one magnetic monolayer, it is possible to construct a magnetic trilayer. While the trilayer of $C_4N_3/MoS_2/BC_3$ and $C_4N_3/MoS_2/C_3N_4$ exhibit half-metallic characteristics, $C_4N_3/MoS_2/C_3N$ possesses a magnetic metallic ground state. Overall, our results reveal that holly structures of BCN crystals are suitable for heterostructure formation even over van der Waals type interaction which significantly changes electronic nature of the constituent layers.

I. INTRODUCTION

Van der Waals (vdW) stacked heterostructures (HTs) have attracted tremendous attention due to their wide applications in the next-generation transistors, optoelectronic, and catalytic technology.[1–5] The vdW HTs which have atomically sharp interfaces, controllable layer components, and minimal trap states when absence of dangling bonds have been extensively investigated in the past few years.[6–12] The relative phase stability can be modified with a vertical HTs that have with ideal band gap, high speed and larger power due to the interlayer interactions.[13,14] Taking advantage of these features, researchers have investigated novel electronic and optoelectronic properties of vdW HTs. The frontier research fields of two-dimensional materials (2DM) are boron carbides (BCs), carbon nitrides (CNs), molybdenum sulfide MoS_2 and its Janus form MoSSe owing to their potential applications in optoelectronics. BCs and CNs have capability due to their atoms which take many different positions, hereby enhance the covalent bondings result in distinctive properties. Therefore, the inspection of new 2D BCs and CNs compounds, many of which have been both experimentally realized and theoretically predicted.

Graphene-like BC_3 monolayer which each carbon hexagon is surrounded by six boron atoms have been synthesized by hot filament chemical vapor deposition methods.[15–17] BC_3 has been produced by chemical synthesis from bulk form within stacked layers that are coupled vdW interaction.[18] BC_3 shows a uniform honeycomb sheet with excellent crystalline quality and its phonon-dispersion curves have been determined both experimentally and theoretically.[15] Monolayer of BC_3 has demonstrated an indirect-gap semiconductor by first-principle calculations.[20–24] 2D polyaniline with stoichiometric formula C_3N and a graphene-like structure in which nitrogen is uniformly distributed reported.[25] Bafekry *et al.* proposed that the electronic properties of C_3N monolayer can be tune via atom adsorption and substitution and applying an electric field/strain.[26–30] Also C_3N demonstrated that can be useful for the catalysis and hydrogen storage,[31] photo-catalyst for water splitting.[32,33] These experimental and theoretical studies lead the engineering and design of new practical applications for C_3N_4 and C_4N_3 in nanoelectronic applications.[34] Owing to C_6N_8, C_8N_6 and C_2N structures have intrinsic vacancies of their crystal structures, spin polarized state expected and they induces various electronic properties with embedding of atom[34–37] Although 2DM hold significant potential for many applications, it will be necessary to tune their intrinsic properties. Several approaches have been considered to change the electronic structure of 2DM such as substitutional doping, defect engineering, application of an electric field or strain, surface functionalization by adatoms, or by altering the edge states.[38–57]

Molybdenum sulfide MoS_2 is also one of the most popular 2DM because of its remarkable optical and electronic properties with 1.9 eV band gap, a low over-potential of 200 mV for H_2 evolution, rich defects, high activity, earth-abundant and robustness[58] and its Janus form MoSSe. In the circumstances, MoS_2 monolayer should be a good alternative co-catalyst on BCs and CNs as vdW HTs. Despite vdW HTs have highly desirable properties, only few works are dealing with the structural and electronic properties of MoS_2 with BC_3N, C_3N, C_3N_4 and C_4N_3 HTs in the literature. For instance, MoS_2 monolayer were coupled into the CN to form MoS_2/C_3N_4 HTs via a facile ultrasonic chemical method and observed that MoS_2 served as electron trapper to extend the lifetime of separated electron-hole pairs.[59] MoS_2/g-C_3N_4 heterojunctions showed higher photocatalytic activity than pure g-C_3N_4 by Li et al.[60] A novel HTs formed by MoS_2-transition metals (Fe, Co, and Ni) on g-C_3N_4 monolayer have been synthesized for obtaining a significant enhancement in the photocatalytic activity for hydrogen production and pollutant disposal.[61] HTs based on MoS_2[62–64] and carbon nitride monolayers have also been considered by DFT in recent years.[65–72] Therefore, motivated by availability of synthesis of vdW HTs, we comprehensively investigated the MoS_2 and MoSSe monolayers with BC_3, C_3N, C_3N_4 and C_4N_3 hetero-bilayer and hetero-trilayer. Our results lead to provide that the electronic properties can show the outstanding properties with constructed of HTs with bilayer and trilayer forms. We expect that this work will attract more experimental and theoretical researchers in near future. These findings also demonstrate that the van der Waals HTs of MoS_2 and MoSSe monolayers on graphitic boron-carbon-nitrides can be considered as promising candidate for future electronics, optoelectronics and spintronics.

II. COMPUTATIONAL METHOD

In this paper, we performed calculations of the electronic structure with geometric optimization, using spin-polarized density functional theory (DFT) as implemented in OpenMX 3.8 package.[73] This code self-consistently finds the eigenfunctions of the Kohn-Sham equations using norm-conserving pseudopotentials,[74] and the wave functions are expanded in a linear combination of multiple pseudoatomic orbitals (LCPAOs).[75,76] The PAO basis functions were specified by $s^2p^2d^1$ for C, B, N, S and Se atoms, while $s^3p^2d^2$ for Mo atom within cutoff radii of basis functions set to the values of seven. We used the Perdew-Burke-Ernzerhof generalized gradient approximation (GGA) for the exchange-correlation functional.[77] The Brillioun zone (BZ) integration was performed by using a Monkhorst-Pack scheme[78] $23 \times 23 \times 1$ k-point mesh for the unit cell and scaled according to the size of the supercell. The kinetic energy cutoff of 350 Ry was used. The geometric structures were relaxed until the force acting on each atom was less than 1 meV/Å. The well-converged structures are obtained with these initial parameters and the obtained ground-state geometric structure was used for the next steps of the calculation. A vacuum space of 25 Å is used for each slab model to eliminate image interactions. The van der Waals (vdW) interaction was included by using the Grimme DFT-D2[79] method for describing long-range vdW interactions.

III. RESULTS

A. Pristine monolayers

The atomic structures of MoS_2, MoSSe, BC_3, C_3N, C_3N_4 and C_4N_3 monolayers after DFT is shown in Fig. 1(a). The lattice constant of MoS_2 and MoSSe monolayers are calculated 3.21 and 3.25 Å, respectively. The vertical distance of S-S (S-Se) is determined 2.99 (3.31) Å and the Mo-S (Mo-Se) bond length is 2.58 (2.56) Å. The BC3 has a lattice constant of 5.17 Å with a planar structure, while the B-C and the C-C bond lengths are 1.56 and 1.42 Å, respectively. These results are consistent with previous calculations.[84,85] In addition, we find the optimized lattice constant, C-C and C-N bond lengths in C_3N to be 4.86 and 1.40 Å, respectively, which are in agreement with previous reports.[25] Moreover, the lattice constant of C_3N_4 is found to be 4.74 Å, with the corresponding bond lengths of C-N are found 1.32 and 1.45 Å as two types, while the angle of N-C-N is 117.4°.[86] Notice that the lattice parameter of C_4N_3 is 4.81 Å, while the bond lengths of C-C and C-N are 1.43 and 1.35 Å, respectively, which are in agreement with previous reports.[87–91] The orbital resolved band structure of BC3, C_3N, C_3N_4 and C_4N_3, MoS_2 and MoSSe monolayers is shown in Fig. 1(b). The BC3 exhibit a semiconducting behavior with an indirect band gap of 0.7 eV.[84,85] The valence band maximum (VBM) which is located at the Γ, is originated from B/C-$p_{x,y}$ orbitals, while the conduction band minimum (CBM), which is located at the **M** point, is dominated by the p_z orbital between the B and C atoms. The p-orbitals have shown at the Γ point, which is very close to the s bonds at the VBM due to local distributions forming hexagonal rings. Notice that the $s-$ and $p-$orbitals can be formed in C-C and B-C bonds in deep energy levels. The C_3N is an indirect semiconductor with a band gap band gap of 0.4 eV. Notice that the VBM is mainly dominated by the N-p_z orbitals, whereas the CBM is originated from C-p_z orbitals.[25,92,93] Similarly, C_3N_4 is a semiconductor with a direct band gap of 1.45 eV, while its VBM and CBM are located at the Γ point. The N-$s, p_{x,y}$ orbitals strongly prominent at the VBM position, while N/C-p_z orbitals have considerable contribution to the CBM[32,33] . The C_4N_3 is a half-metal and has 1 μ_B magnetic moment in the ground state. The VBM of dominated from the C-p_z and N-$p_{x,y}$ orbitals while the CBM is originated from N-$p_{x,y}$ orbitals (see Fig. 2(b)). Clearly, the N-$p_{x,y}$ orbitals around the Fermi-

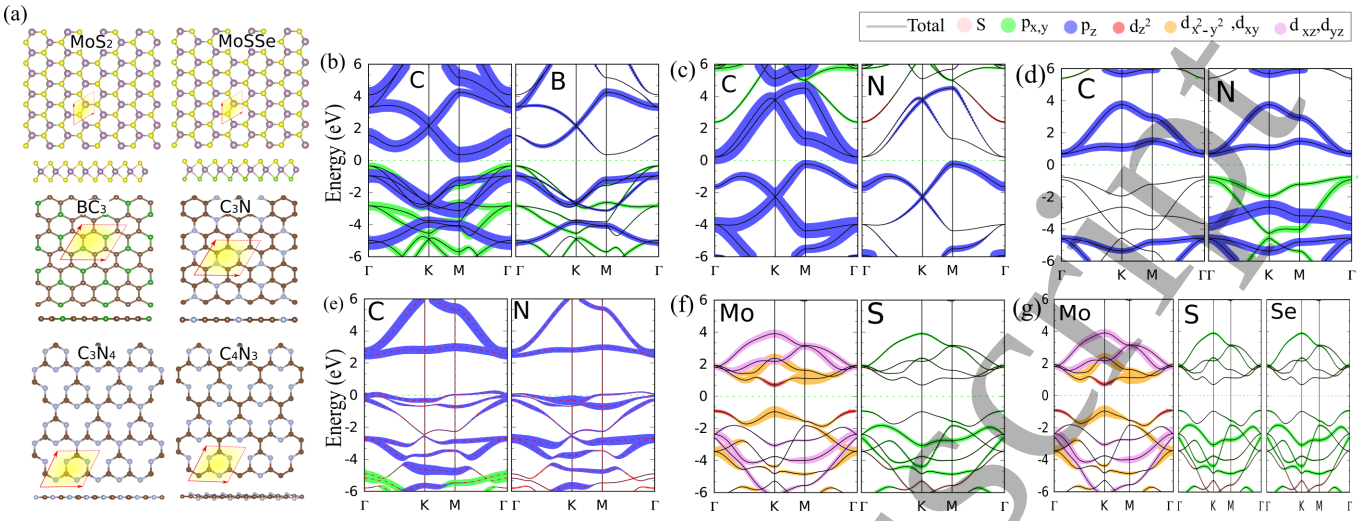

Figure 1. (a) Atomic structures and (b-g) orbital resolved band structure of MoS_2, MoSSe, BC_3, C_3N, C_3N_4 and C_4N_3 monolayers with its hexagonal primitive unit cell indicated by the red parallelogram. Violet, yellow, light green, dark green, brown and blue balls represent W, S, Se, B, C and N atoms, respectively. The zero of energy is set to Fermi-level.

level cause the half-metallicity and the magnetism.[87–89] We also confirm that the MoS_2 and MoSSe monolayers are a semiconductor with direct band gap of 1.65 eV and 1.6 eV, respectively, we can found that the VBM and CBM are located at the K-point.

B. Structre properties of heterostructures

For the investigation of heterostructures (HTs), we select the $3 \times 3 \times 1$ supercell of MoS_2 on top of a $2 \times 2 \times 1$ supercell of BC (BC3) and CNs (C_3N, C_3N_4 and C_4N_3) which is benefit to forming possible structures. Also the HTs composed of MoSSe with C_3N and C_3N_4 monolayers are considered. The hetero-bilayer and hetero-trilayer composed of MoS_2, BC, and CNs monolayers, are also explored. The MoS_2/C_3N hetero-bilayer contains 59 atoms (9 Mo, 18 S, 24 C and 8 N) and the $BC_3/MoS_2/C_3N$ hetero-trilayer contains 91 atom (9 Mo, 18 S, 48 C, 8 B and 8 N). In addition $MoS_2/C_3N/MoS_2$ hetero-trilayer composed of 86 atom (18 Mo, 36 S, 24 C and 8 N). The lattice mismatch (δ) is defined as $\delta = \frac{|a_{up}-a_{dn}|}{a_{dn}} \times 100\%$, where a_{up} and a_{dn} represent the lattice constants of upper and down layers, respectively. The lattice mismatch between MoS_2 (MoSSe) with C_3N, C_3N_4, C_4N_3 and BC_3 monolayers are determined to be 0.93% (0.31%), 1.55% (2.77%), 0.1% (1.33%) and 7.37% (6.05%), respectively. The lattice mismatches for MoSSe on C_3N and C_3N_4 monolayers are calculated 2.77% and 1.33%, respectively. These lattice mismatch reveal the small distortions in the structures of MoS_2 and MoSSe with CNs. In order to investigate the structural stability of MoS_2/BCN, the energies of different stacking are calculated. The energetically feasible stackings are obtained by placing the BC and CNs monolayers on the MoS_2 surface with four stacking patterns (AA, AB, BA, BB). The AA stacking comprise of CN hexagonal ring directly above MoS_2 hexagonal ring and the hole center of BC and CNs sheets directly above a next-nearest-neighbor MoS_2 hexagonal ring. On the other hand, the AB stacking is formed such that the center of a CN hexagonal ring reside directly above S atom and the center of the hole of BCs and CNs sheets directly above a next-nearest-neighbor S atom.

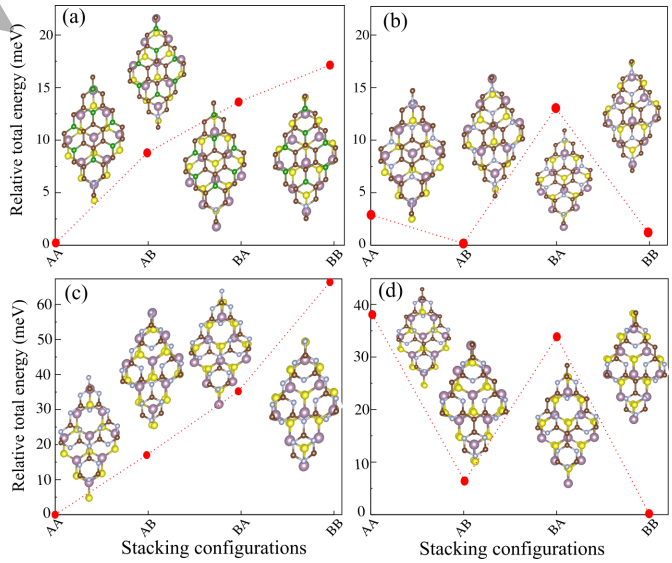

Figure 2. Relative total energies of four stacking patterns (AA, AB, BA, BB) with top views for MoS_2/BC and MoS_2/CN HTs. Total energy of stacking pattern (a) BB (MoS_2/BC_3), (b) BA (MoS_2/C_3N), (c) BB (MoS_2/C_3N_4) and (d) AA (MoS_2/C_4N_3) are sets to zero.

The relative total energies of BC_3, C_3N, C_3N_4, C_4N_3 are reported in Figs. 2(a-d) in order to quantitatively specify the structural stability of four stacking patterns.

We found that the variation of relative total energies of four stacking types is not significant. The most stable stacking is determined by the minimum total energy among the four different configurations, where the top views of stacking pattern is shown in the inset in Fig. 2. The lowest total energy are determined at BB (MoS_2/BC_3), BA (MoS_2/C_3N), BB (MoS_2/C_3N_4), AA (MoS_2/C_4N_3) than other tree types. The lattice constants (a, b) are calculated for MoS_2/BC_3 (10.078, 10.080), MoS_2/C_3N (9.717, 9.718), MoS_2/C_3N_4 (9.505, 9.476) and MoS_2/C_4N_3 (9.606, 9.615) based on the stable configurations of MoS_2/BC and MoS_2/CN (see Table I). For investigation of thermal and dynamical stability of different HTs, we have performed the *ab-initio* molecular dynamics (AIMD) simulation for different HTs at 500 K. AIMD simulations for the MoS_2/C_3N, MoS_2/C_3N_4 and MoS_2/C_4N_3 HTs at 500 K are shown in Fig. S4 (a-c), respectivelly, where the top and side views of optimized structures are indicated in the inset. The thermal dynamic investigations are started with the optimized structures at 0 K and the temperature was increased to 500 K within 2 ps. As can be noticed from the snapshots, apart from minor distortions, the crystal structures of these HTs are preserved, further confirming the stability even at least up to 500 K. Our results indicate that these HTs are thermally stable.

The binding energy (E_b) of the constructed HTs is calculated using the given formula as below:

$$E_b = E_{tot} - E_{MoS_2} - E_{BCN} \qquad (1)$$

where E_{tot}, E_{MoS_2} and E_{BCN} are the total energies of the optimized MoS_2/BCN HTSs, MoS_2 monolayer, and BCN (BC3, C_3N, C_3N_4 and C_4N_3) layers, respectively. The total energy of the studied monolayers are computed using the same supercell that the one in the calculation of the vdW HTs.

The binding energy and the structural parameters including bond length, interlayer distance and buckling are listed in Table I. The binding energies are determined to be -15.32 meV/$Å^2$ (MoS_2/BC_3), -15.21 meV/$Å^2$ (MoS_2/C_3N), -15.11 meV/$Å^2$ (MoS_2/C_3N_4) and -14.98 meV/$Å^2$ (MoS_2/C_4N_3). For the MoSSe/C_3N and MoSSe/C_3N_4, the binding energy values are calculated -15.18 and -15.11 meV/$Å^2$, respectively. The interlayer distance between MoS_2 (MoSSe) and BC and CNs monolayers are found as the range of 3.14-3.33 Å. These results indicate the weak vdW interaction between the two layers. The difference density charge, the planar averaged difference charge density, and a quantitative results of charge distribution for the MoS_2/BC_3 and MoS_2/CNs are given at supplementary information Fig. S1(a). While the blue colors show the charge accumulation, the red colors denote the charge depletion. The difference charge density Δ_ρ is defined as;

$$\Delta_\rho = \rho_{MoS_2/BCN} - \rho_{BCN} - \rho_{MoS_2}, \qquad (2)$$

where $\rho_{MoS_2/BCN}$, ρ_{BCN}, and ρ_{MoS_2} represents the charge densities of the MoS_2/BCN HTs and free-standing BC or CNs and MoS_2, monolayers, respectively. We can see that due to the interaction between two layers an charge redistribution occurs at the MoS_2/CN interface region is observed, while there is almost no charge change in the MoS_2 layer. According to our results, the charge accumulation largely occurs in the central region of inter-

Table I. Structural parameters of MoS_2/BC and MoS_2/CN HTs include the a and b are lattice constants, t is the thickness of MoS_2, h is the interlayer distance, δz is the buckling which stem from the difference between the smallest and largest z coordinates of atoms, (d_{B-C}), (d_{C-N}), (d_{C-C}) and (d_{Mo-S}) are the bond lengths of between B-C, C-N, C-C, and Mo-S atoms, respectively. All distance and angles are given in Å. The E_b is binding energy. The binding energy is shown is given in meV/$Å^{-2}$.

HTS	a	b	E_b	t	h	δz	$d_{B(C)-C(N)}$	d_{C-C}	d_{Mo-S}
BC_3	10.078	10.080	-15.32	3.098	3.214	0.388	1.525	1.401	2.483
C_3N	9.717	9.718	-15.21	3.164	3.330	0.0	1.403	1.402	2.447
C_3N_4	9.505	9.476	-15.11	3.213	3.137	1.331	1.337-1.468	-	2.428
C_4N_3	9.606	9.615	-14.98	3.190	3.317	0.714	1.351	1.442	2.445

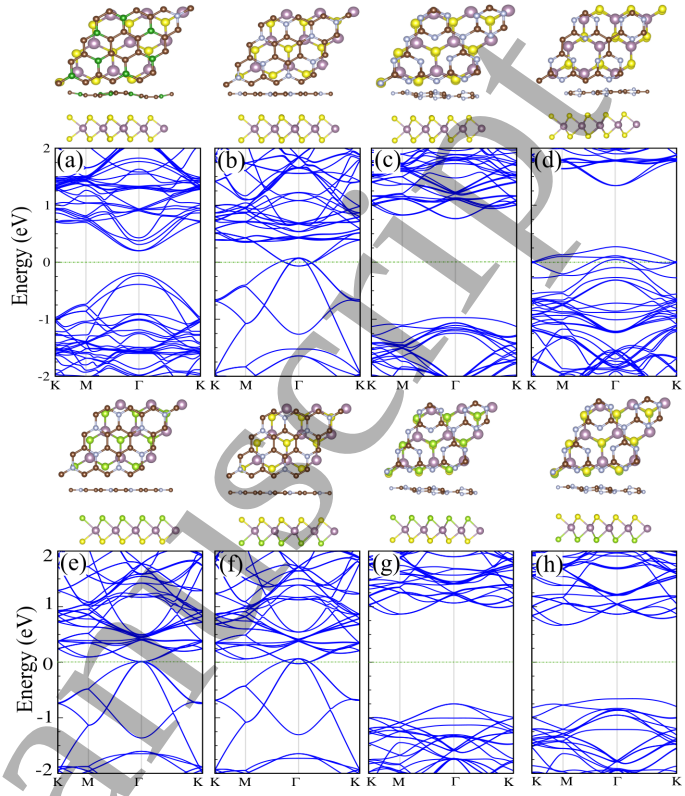

Figure 3. Electronic band structure of (a) MoS_2/BC_3, (b) MoS_2/C_3N, (c) MoS_2/C_3N_4, (d) MoS_2/C_4N_3, (e) MoSSe/C_3N, (f) MoSSe/C_3N, (g) MoSSe/C_3N_4 and (h) MoSSe/C_3N_4 HTs with two different face of Janus MoSSe. The zero of energy is set to Fermi-level. Optimized structures are shown on the top panel.

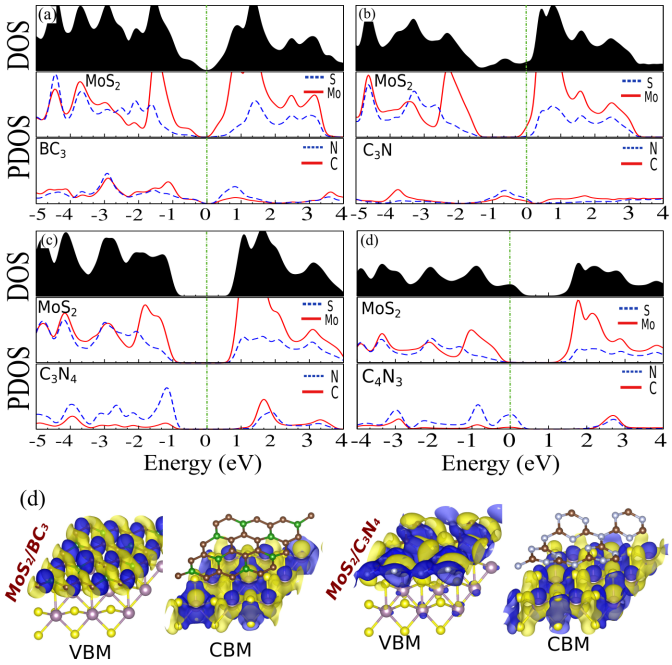

Figure 4. DOS and PDOS of (a) MoS_2/BC_3, (b) MoS_2/C_3N, (c) MoS_2/C_3N_4, (d) MoS_2/C_4N_3 HTs. The zero of energy is set to Fermi-level. (e) Charge density of VBM (left panel) and CBM (right panel) of MoS_2/BC_3 and MoS_2/C_3N_4, respectively. The accumulation and depletion of charge densities represent the blue and yellow colors, respectively.

face, and the charge depletion mostly stem from the two boundaries of interface. To explore the charge transfer more clearly, the planar-averaged difference charge density along the z-direction is shown in Fig. S1(b). Here, the positive values indicate electron accumulation, while the negative values indicate the electron depletion. We found that the charge transfer from BCNs to MoS_2 layer occurs at the interface region. In order to provide visible guidance for experimental observations, first-principles DFT calculations were performed to calculate the STM image (see Fig. S2). To correlate the STM image with the corresponding atomistic structure, we overlayed it with the MoS_2/BCN. The simulated STM images shows that the brightness of CN in MoS_2/CN is much weaker than that of the free-standing monolayer form. Beside, the brightness of MoS_2 in MoS_2/CN is also much stronger than the isolated MoS_2.

C. Hetero-bilayer

Some fundamental parameters of these HTs, such as interface bonding, charge transfer, band gap change, and band alignment, remain unknown. For device applications based on HTs, understanding these fundamental issues is highly important and essential. In this work, we studied electronic properties of bilayer MoS_2/BC_3, MoS_2/C_3N, MoS_2/C_3N_4 and MoS_2/C_4N_3

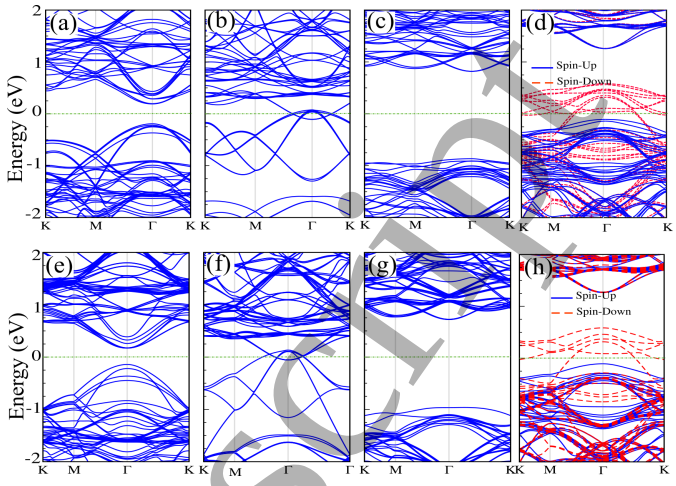

Figure 5. Electronic band structure of trilayer HTs including of (a) $BC_3/MoS_2/BC_3$, (b) $C_3N/MoS_2/C_3N$, (c) $C_3N_4/MoS_2/C_3N_4$, (d) $C_4N_3/MoS_2/C_4N_3$, (e) $MoS_2/BC_3/MoS_2$, (f) $MoS_2/C_3N/MoS_2$, (g) $MoS_2/C_3N_4/MoS_2$ and (h) $MoS_2/C_4N_3/MoS_2$. The zero of energy is set to Fermi-level. Optimized structures are shown in the top of panel.

HTs using first-principle calculations. The electronic band structure of MoS_2/BC_3, MoS_2/C_3N, MoS_2/C_3N_4 and MoS_2/C_4N_3 HTs are shown in Fig. 3(a-d). The top and side views of optimized structures are shown in the top panel. And corresponding the density of states (DOS) and partial DOS (PDOS) of these vdW HTs are shown in Fig. 4(a-d). According to our results, buckling instabilities are caused by out-of-plane displacements due to different equilibrium interlayer separations for stacking configurations for MoS_2/BC_3, MoS_2/C_3N_4 and MoS_2/C_4N_3, while MoS_2/C_3N show flat (see Figs. 3(a-d)). Our result show that the MoS_2/BC_3 is a semiconductor possessing a direct band gap of 0.4 eV whose VBM and CBM reside at the Γ-point. The band gap of the HT is smaller than those of monolayers MoS_2 (1.65 eV) and BC_3 (0.7 eV) indicating the electron charge transfer from VBM to CBM in this HT becomes much easier. Notice that the VBM is formed by the Mo-*d* orbitals, while the CBM is attributed to the the hybridization of Mo-*d* and N-*p* (see Fig. 4(a)). Owing to the strongly interaction between C_3N with MoS_2, the band gap of the MoS_2/BC_3 is interestingly removed and exhibit a metallic characteristic.[83] DOS and PDOS results demonstrated that both of the MoS_2 and C_3N_4 affect to their the electronic states distribution near the Fermi level due to strong interaction effect between the two layers. We can see that this metallicity is mainly originates from Mo-d orbital of MoS_2. Notice that the MoS_2/C_3N_4 show a direct semiconductor with 1.74 eV band gap. Moreover, the VBM and CBM is originated from N-*p* and Mo-*d* orbitals of C_3N_4 and MoS_2, respectively. This circumstance indicates that a easier charge transfer between the two constituents and much wider visible-optical re-

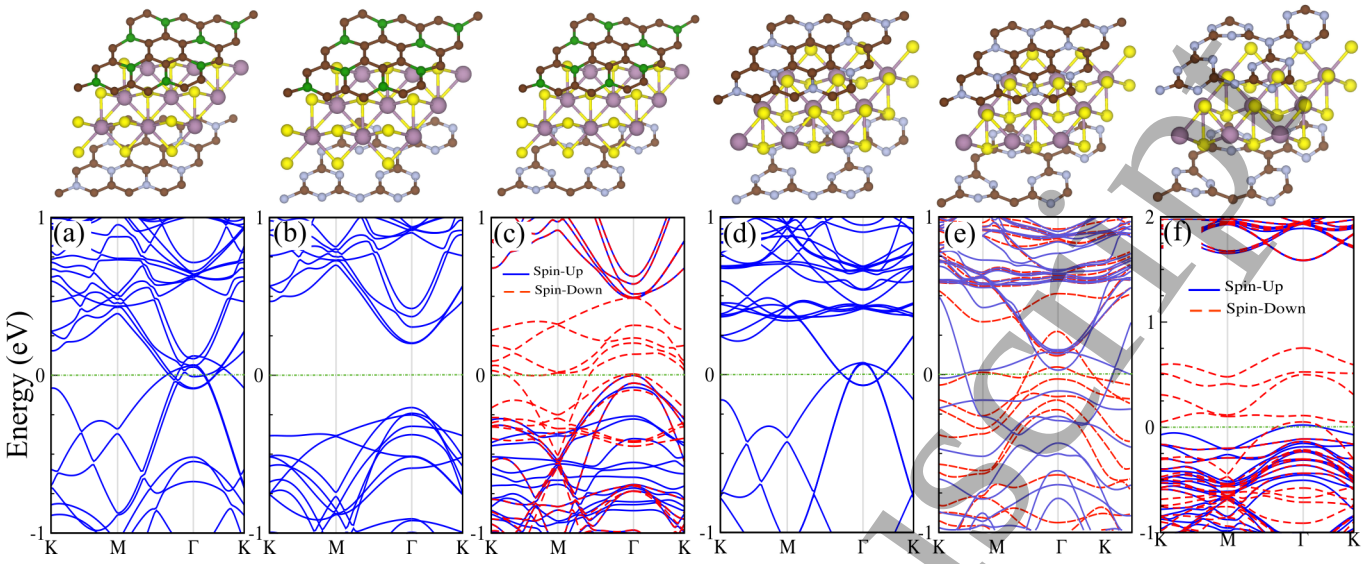

Figure 6. Electronic band structure of trilayer HTs including of (a) $C_3N/MoS_2/BC_3$, (b) $C_3N_4/MoS_2/BC_3$, (c) $C_4N_3/MoS_2/BC_3$, (d) $C_3N/MoS_2/C_3N_4$, (e) $C_3N/MoS_2/C_4N_3$ and (f)$C_4N_3/MoS_2/C_3N_4$. The zero of energy is set to Fermi-level. Optimized structures are shown in the top of panel.

sponse range than the isolated MoS_2 or C_3N_4 monolayers. Interestingly the magnetic properties of C_4N_3 (is half-metal in natural state) is eliminated when it makes a HTS with MoS_2 and become a metal. Moreover, in MoS_2/C_4N_3, the state at Fermi-level belongs to the N-p orbitals of C_4N_3 yielding the metallic character (see Fig. 4(d)). Our results for MoS_2/C_4N_3 show that the states around Fermi-level mainly originate from of the N-p orbital of C_4N_3. The half-metallicity of C_4N_3 with decorating on MoS_2 is diminished and MoS_2/C_4N_3 transform to a metal. N-2p and Mo-4d orbitals of MoS_2/C_3N_4 contribute to the electronic states around the Fermi level. Thus, comparing with the MoS_2 or C_3N_4 monolayers, the MoS_2/C_3N_4 may be a more appropriate photocatalytic candidate. The charge density of VBM (left panel) and CBM (right panel) of MoS_2/BC_3 and MoS_2/C_3N_4, respectively, are shown in Fig. 4(d). The blue and yellow color represent the accumulation and depletion charge densities, respectively.

The electronic properties of Janus MoSSe on C_3N and C_3N_4 HTs are shown in Figs. 3(e-h), while the optimized structures of the these HTs are shown in the top panel. The structural parameters including bond length, interlayer distance and buckling for Janus MoSSe with C_3N are present here. The interlayer distance are determined for $MoSSe/C_3N$ (3.914 Å), $MoSeS/C_3N$ (3.822 Å), $MoSSe/C_3N_4$ (4.030 Å) and $MoSeS/C_3N_4$ (3.963 Å). It also proof of the weak vdW interaction between the two layers. The planar structure of C_3N is preserved in both system of $MoSSe/C_3N$ and $MoSeS/C_3N$, while we can see buckling of 0.68 and 0.72 Å, respectively, for $MoSSe/C_3N_4$ and $MoSeS/C_3N_4$. Notice that in the $MoSSe/C_3N$ (see Fig. 3(e)), the VBM and CBM tangent each to gather in Fermi-level, while for $MoSeS/C_3N$ (see Fig. 3(f)) the energy bands around the Fermi-level cross each other and both systems shows a metallic character. Whereas, $MoSSe/C_3N_4$ and $MoSeS/C_3N_4$, are indirect semiconductor with 1.6 and 1.3 eV band gaps (see Figs. 3(g) and 3(h), respectively). Notice that the VBM and CBM are located at Γ and M points, respectively.

D. Hetero-trilayer

In this section, we investigate the electronic properties of $BCN/MoS_2/BCN$ and $MoS_2/BCN/MoS_2$ HTs. The electronic band structure of $BCN/MoS_2/BCN$ and $MoS_2/BCN/MoS_2$ HTs are shown in Figs. 5(a-h). The optimized structures of these HTs are shown on the top of panel. We can see that $BC_3/MoS_2/BC_3$ and $MoS_2/BC_3/MoS_2$, are direct semiconductor with 0.38 and 0.3 eV band gaps, respectively, while the VBM and CBM are located at Γ point. Notice that the $C_3N/MoS_2/C_3N$ and $MoS_2/C_3N/MoS_2$, exhibits a metallic character. Our result show that the $C_3N_4/MoS_2/C_3N_4$ and $MoS_2/C_3N_4/MoS_2$ are semiconductor and have a dire band gap with values of 1.69 eV and 1.66 eV that VBM and CBM are located at Γ point. In addition, we see an indirect band gap of 1.74 eV and 1.70 eV for these HTs. The electronic structure of $C_4N_3/MoS_2/C_4N_3$ and $MoS_2/C_4N_3/MoS_2$ reveals half-metal state where the energy bands are split into ↑ and ↓ spin channels. While induced magnetic moment into these HTs are 8 and 4 μ_B, respectively, which is due to the magnetic properties of C_4N_3.

Here, we investigate the structure and electronic properties of trilayer HTs including of one monolayer of MoS_2 that sandwiched between two layers with different types

of BCN monolayers. The electronic band structure of these systems are shown in Figs. 6(a-h). Also the top and side views of optimized structures are shown in the top of panel. The electronic band structure and corresponding density of states (DOS) and partial density of states (PDOS) of six studied HTSs are shown in Fig. 1(b) and Fig. 2, respectively. From the Fig. 6(a) and (d), respectively, for the $C_3N/MoS_2/BC_3$ and $C_3N/MoS_2/C_3N_4$, we can see that, in comparison to the pristine monolayers, the semiconducting behavior of is diminished and becomes a metal. The $C_3N_4/MoS_2/BC_3$ is a direct semiconductor with 0.4 eV band hap, where the VBM and CBM are located at Γ-point (see Fig. 6(b)). Interestingly, $C_4N_3/MoS_2/BC_3$ and $C_4N_3/MoS_2/C_3N_4$ becomes a half-metal where the energy bands are split into ↑ and ↓ spin channels and induced 4 and 3.8 μ_B magnetic moments, respectively (see Fig. 6(c) and Fig. 6(h), respectively). The electronic structure of $C_3N/MoS_2/C_4N_3$ reveals ferromagnetic-metal and the degeneracy of both spin channels are broken which results in a magnetic moment of 3.5 μ_B (see Fig. 6(e)). Therefore we found that the magnetic properties of C_4N_3 is preserved in these HTS. The electronic structure results of the above three HTSs show that the electronic structure of MoS_2 is not preserved when it is put on BCN monolayers.

IV. CONCLUSION

By performing *ab-initio* calculations, the structural and electronic properties of van der Waals heterostructures (HTs) constructed by MoS_2/BC_3, MoS_2/C_3N, MoS_2/C_3N_4, MoS_2/C_4N_3 and those using Janus MoSSe instead of MoS_2 were investigated. The electronic band structure calculations and the corresponding partial density of states revealed the significant changes driven by quite strong layer-layer interaction between the constitutive layers. Although, free-standing monolayers were found to be semiconductors, the MoS_2/C_3N and MoS_2/C_4N_3 bilayer HTs were shown to display metallic behavior as a consequence of transfer of charge carriers between two constituent layers. In addition, it was found that in $MoSSe/C_3N$ bilayer HT, the degree of metallicity is affected by the interface chalcogen atom type that when Se atoms are facing to C_3N layer, the overlap of the bands around the Fermi level is smaller. Moreover, the half-metallic magnetic C_4N_3 was calculated to form magnetic half-metallic three-layer HT with MoS_2 independent of the stacking sequence. Furthermore, for the three-layer HTs in which MoS_2 is encapsulated by two different monolayers, it was revealed that at least with one magnetic monolayer, it is possible to construct a magnetic three-layer HT. While the three-layer HTs of $C_4N_3/MoS_2/BC_3$ and $C_4N_3/MoS_2/C_3N_4$ were found to exhibit half-metallic structures, $C_4N_3/MoS_2/C_3N$ possesses a magnetic metallic ground state. Our results revealed that holly structures of BCN crystals are suitable for heterostructure formation even over van der Waals type interaction which significantly changes electronic nature of the constituent layers.

V. ACKNOWLEDGEMENTS

This work has supported by the National Research Foundation of Korea(NRF) grant funded by the Korea government(MSIT)(NRF-2017R1A2B2011989). M.Y. is supported by the Flemish Science Foundation (FWO-Vl) by a postdoctoral fellowship.

VI. DATA AVAILABLE ON REQUEST FROM THE AUTHORS

The data that support the findings of this study are available from the corresponding author upon reasonable request.

* bafekry.asad@gmail.com
† mitragh@skku.edu

[1] F. Bonaccorso, L. Colombo, G. Yu, M. Stoller, V. Tozzini, A. C. Ferrari, R. S. Ruoff, V. Pellegrini, *Sci.* 2015, **347**, 1246501.
[2] C. Tan, H. Zhang, *Nat. Commun.* 2015, **6**, 7873.
[3] B. Luo, G. Liu, L. Wang, *Nanoscale* 2016, **8**, 6904.
[4] C. Tan, X. Cao, X.-J. Wu, Q. He, J. Yang, X. Zhang, J. Chen, W. Zhao, S. Han, G.-H. Nam, M. Sindoro, H. Zhang, *Chem. Rev.* 2017, **117**, 6225.
[5] J. Di, J. Xiong, H. Li, Z. Liu, *Adv. Mater.* 2018, **30**, 1704548.
[6] H. Li , J. Wu , Z. Yin H. Zhang *Acc. Chem. Res.* 2014, **47**, 1067.
[7] W. Su , H. Dou , J. Li , D. Huo , N. Dai, L. Yang , *RSC Adv.* 2015, **5**, 82924.
[8] M. Buscema , G. A. Steele , H. S. J. van der Zant, A. Castellanos-Gomez, *Nano Res.* 2014, **7**, 561.
[9] W. Su , H. Dou , D. Huo , N. Dai, L. Yang, *Chem. Phys. Lett.* 2015, **635**, 40.
[10] S. Mouri , Y. Miyauchi K. Matsuda, *Nano Lett.* 2013, **13**, 5944.
[11] X. Zhou , W. Feng , S. Guan , B. Fu , W. Su, Y. Yao, *J. Mater. Res.* 2017, **32**, 2993.
[12] Y. Deng , Z. Luo , N. J. Conrad , H. Liu , Y. Gong , S. Najmaei , P. M. Ajayan , J. Lou , X. Xu, P. D. Ye, *ACS Nano* 2014, **8**, 8292.
[13] J. Yan , Y. Hao , Y. Cui , J. Zhang , Y. Zou , W. Zhang , G. Yu , J. Zheng , W. Xu, D. Zhu, *J. Mater. Chem. C* 2018, **6**, 12976.
[14] K. H. Chan , S. M. Ng , H. F. Wong , C. W. Leung, C. L. Mak, *Phys. Status Solidi A* 2019, **216**, 1800829.

[15] H. Yanagisawa, T. Tanaka, Y. Ishida, M. Matsue, E. Rokuta, S. Otani, C. Oshima, *Phys. Rev. Lett.* 2004, **93**, 177003.
[16] H. Tanaka, Y. Kawamata, H. Simizu, T. Fujita, H. Yanagisawa, S. Otani, C. Oshima *Solid State Commun.* 2005, **136**, 22.
[17] H. Yanagisawa, T. Tanaka, Y. Ishida, M. Matsue, E. Rokuta, S. Otani, C. Oshima, *Phys. Rev. B* 2006, **73**, 045412.
[18] J. Kouvetakis, R. B. Kaner, M. L. Sattler, N. Bartlett, *J. Chem. Soc. Chem. Commun.* 1968, **24**, 1758.
[19] K. S. Novoselov, D. Jiang, F. Schedin, T. J. Booth, V. V. Khotkevich, S. V. Morozov, A. K. Geim, *PNAS* 2005, **102**, 10451.
[20] D. Tomanek, R. M. Wentzcovitch, S. G. Louie, M. L. Cohen, *Phys. Rev. B* 1988, **37**, 3134.
[21] T. Sasaki, M. Akaishi, S. Yamaoka,Y. Fujiki, T. Oikawa, *Chem. Mater.* 1993, **5**, 695.
[22] A. Bafekry, S. Farjami Shayesteh, M. Ghergherehchi, F. M. Peeters, *J. Appl. Phys.* 2019, **126**, 144304.
[23] Y. Ding, Y. Wang, J. Ni, *Appl. Phys. Lett.* 2009, **94**, 073111.
[24] A. Bafekry, *Phys. E Low-Dimensional Syst. Nanostruct.* 2020, **118**, 113850.
[25] J. Mahmood, E. K. Lee, M. Jung, D. Shin, H. J. Choi, J. M. Seo, S. M. Jung, D. Kim, F. Li , M. S. Lah, N. Park , H. J. Shin, J.H. Oh, J. B. Baek, *PNAS* 2016, **113**, 7414.
[26] A. Bafekry, S. Farjami Shayesteh, F. M. Peeters, *J. Phys. Chem. C* 2019 **123**, 12485.
[27] A. Bafekry, C. Stampfl, S. F. Shayesteh, and F. M. Peeters, *Adv. Elect. Mater.* 2019, **5**, 1900459.
[28] A. Bafekry, S. Farjami Shayesteh, and F. M. Peeters, *Phys. Chem. Chem. Phys.* 2019, **21**, 21070.
[29] A. Bafekry, M. Ghergherehchi, S. Farjami, F. M. Peeters, *Chem. Phys.* 2019 **562**, 110442.
[30] A. Bafekry, C. Stampfl, and S. Farjami Shayesteh, *ChemPhysChem* 2020, **21**, 164 (2020).
[31] O. Faye, T. Hussain, A. Karton, J. Szpunar, *Nanotechnol.* 2018, **30**, 75404.
[32] Zh. Guizhi, L. Kun, S. Qiang, K. Yoshiyuki, J. Puru, *Comput. Mater. Sci.* 2014, **81**, 275.
[33] X. Li, S. Zhang and Q. Wang, *Phys. Chem. Chem. Phys.* 2013, **15**, 7142.
[34] A. Bafekry, C. Stampfl, B. Akgenc, and M. Ghergherehchi, *Phys. Chem. Chem. Phys.* 2020, **22**, 2249.
[35] A. Bafekry, C. Stampfl, B. Akgenc, B. Mortazavi, M. Ghergherehchi, C. V. Nguyen, *Phys. Chem. Chem. Phys.* 2020, **22**, 6418.
[36] A. Bafekry, C. Stampfl, M. Ghergherehchi, and S. F. Shayesteh, *Carbon* 2020, **157**, 371.
[37] A. Bafekry, S. F. Shayesteh, and F. M. Peeters, *J. Appl. Phys.* 2019, **126**, 215104.
[38] M. M. Obeid, H. R. Jappor, K. Al-Marzoki, D. Hoat, T. V. Vu, S. J. Edrees, Z. M. Yaseen, and M. M. Shukur, *Comput. Mater. Sci.* 2019, **170**, 109201.
[39] S. Wang, Ch. Ren, H. Tian, J. Yu, M Sun, *Phys. Chem. Chem. Phys.* 2018, **20**, 13394.
[40] *J. Phys. D: Appl. Phys.* 2018, **51**, 105004.
[41] A. O. M. Almayyali, B. B. Kadhim, H. R. Jappor, *Phys. E: Low-dimensional Syst. Nanost.* 2020, **118**, 113866.
[42] Y. F. Luo, Y. Pang, M. Tang, Q. Song, M. Wang, *Comput. Mater. Sci.* 2019, **156**, 315.
[43] M. Yagmurcukardes, C. Sevik, and F. M. Peeters, *Phys. Rev. B* 2019, **100**, 045415.
[44] A. Bafekry, M. Ghergherehchi, and S. Farjami Shayesteh, *Phys. Chem. Chem. Phys.* 2019, **21**, 10552.
[45] T. V. Vu, N. V. Hieu, H. V. Phuc, N. N. Hieu, H. Bui, M. Idrees, B. Amin, and C. V. Nguyen, *Appl. Surf. Sci.* 2020, **507**, 145036.
[46] D. D. Vo, T. V. Vu, N. V. Hieu, N. N. Hieu, H. V. Phuc, N. T. T. Binh, L. T. T. Phuong, M. Idrees, B. Amin, and C. V. Nguyen, *Phys. Chem. Chem. Phys.* 2019, **21**, 25849.
[47] A. Bafekry, C. Stampfl, and F. M. Peeters, *Sci. Rep.* 2020, **10**, 1 (2020).
[48] H. U. Din, M. Idrees, A. Albar, M. Shafiq, I. Ahmad, C. V. Nguyen, B. Amin, *Phys. Rev. B* 2019, **100**, 165425.
[49] D. Kiymaz, M. Yagmurcukardes, A. Tomak, H. Sahin, R. T. Senger, F. M. Peeters, H. M. Zareie, C. Zafer, *Nanotechnol.* 2016, **27**, 455604.
[50] M. M. Obeid, H. R. Jappor, K. Al-Marzoki, I. A. Al-Hydary, S. J. Edrees, M. M. Shukur, *RSC Advances* 2019, **9**, 33207.
[51] M. Shahrokhi and C. Leonard, *J. Alloys and Compounds* 2017, **693**, 1185.
[52] A. Bafekry, B. Mortazavi, and S. F. Shayesteh, *J. Magnetism and Magnetic Mater.* 2019, **491**, 165565.
[53] M. Yagmurcukardes, *Phys. Rev. B* 2019, **100**, 024108.
[54] M. Shahrokhi, *Appl. Surf. Sci.* 2016, **390**, 377.
[55] M. Yagmurcukardes, S. Ozen, F. Iyikanat, F. M. Peeters, H. Sahin, *Phys. Rev. B* 2019, **99**, 205405.
[56] B Mortazavi, A Bafekry, M Shahrokhi, T Rabczuk, X Zhuang, *Materials Today Energy*, 2020, *16*, 100392.
[57] A. Bafekry, M. Neek-Amal, F. M. Peeters, *Phys. Rev. B* 2020, *101*, 085417.
[58] C. Feng, J. Ma, H. Li, R. Zeng, Z. Guo, H. Liu, *Materials Research Bulletin* 2009, **44**, 1811.
[59] Q. Li, N. Zhang, Y.Yang, G. Wang, N. Guozhong, D. H. L. Dickon, *Langmuir* **30**, 2014, 8965.
[60] J. Li, E. Liu, Y. Ma, X. Hu, J. Wan, L. Sun, J. Fan, *Appl. Surf. Sci.* **364**, 2016.
[61] K. Li, Y.Z. Lin, Y. Zhang, M. L. Xu, L. W Liu, F. T. Liu, *J. Mater. Chem. C* **13211-13217**, 2019.
[62] M. Farkous, M, M. Bikerouin, D. V. Thuan, Y. Benhouria, M. El-Yadri, E. Feddi, H. Erguig, F. Dujardin, C. V. Nguyen, N. V. Hieu, Nguyen, H. D. Bui, N. H. Hieu, H. V. Phuc, *Phys. E Low-Dimensional Syst. Nanostruct.* **116**, 113799 2020.
[63] B. Amin, T. P. Kaloni, G. Schreckenbach, M. S. Freund *Appl. Phys. Lett.* 2016, **108**, 063105.
[64] J. B Lee, Y. R. Lim, A. K. Katiyar, W. Song, J. Lim, S. Bae, T.W. Kim, S. K. Lee, J. H. Ahn, *Adv. Mater.* 2019, **31**, 1904194.
[65] M. M. Obeid, *Appl. Surf. Sci.* 2020, **508**, 144824.
[66] A. Bafekry, B. Akgenc, S. F. Shayesteh, B. Mortazavi, *Appl. Surf. Sci.* 2020, **505**, 144450.
[67] S. M. Mozvashi, S. I. Vishkayi, M. B. Tagani, *Phys. E: Low-dimensional Syst. Nanostruct.* 2020, **118**, 113914.
[68] Zh. Guan, Ch.-Sh. Lian, Sh. Hu, Sh. Ni, Jia Li, W. Duan, *J. Phys. Chem. C* 2017, **121**, 3654.
[69] Ch. Yu, X. Cheng Ch. Wang, Zh. Wang, *Phys. E Low-Dimensional Syst. Nanostruct.* 2019, **110**, 148.
[70] D. Cheng, X. Lei, Y. Wang, Sh. Zhong, G. Liu, B. Xu, Ch. Ouyang, *Appl. Surf. Sci.* 2019, **497**, 143809.
[71] A. Bafekry and M. Neek-Amal, *Phys. Rev. B* 2020, **101**, 085417.
[72] A. Bafekry, M. Ghergherehchi, C. Stampfl, *Nanotechnol.* 2020, **101**, 085417.

[73] T. Ozaki, K. Nishio, H. Kino, *Phys. Rev. B* 2010, **81**, 035116.
[74] N. Troullier, J. Martins, *Phys. Rev. B* 1991, **43**, 1993.
[75] T. Ozaki, *Phys. Rev. B* 2003, **67**, 155108.
[76] T. Ozaki, H. Kino, *Phys. Rev. B* 2004, **69**, 195113.
[77] J. P. Perdew, K. Burke, M. Ernzerhof, *Phys. Rev. Lett.* 1996, **77**, 3865.
[78] Monkhorst, H. J. Pack, J. D. *Phys. Rev. B* 1976, **13**, 5188.
[79] S. Grimme, *Comput. Chem.* 2006, **27**, 1787.
[80] J. Tersoff, D. R. Hamann, *Phys. Rev. Lett.* 1983, **50**, 1998.
[81] I. Horcas, R. Fernandez, J. M Gomez-Rodriguez, J. Colchero, J. Gomez-Herrero, A. M. Baro, *Rev. Sci. Instr.* 2007, **78**, 013705.
[82] K. M. Mak, Ch. Lee, J. Hone, J. Shan, T. F. Heinz, *Phys. Rev. Lett.* 2010, **105**, 136805.
[83] Y. Yang, Zh. Wang, *RSC Adv.*, 2019, **9**, 19837.
[84] Y. Ding, Y. Wang, J. Ni, *J. Phys. Chem. C* 2010, **114**, 12416.
[85] S. Behzad, *Surf. Sci.* 2017, **665**, 37.
[86] E. Kroke, M. Schwarz, E. Horath-Bordon, P. Kroll, Br. Noll and A. D. Norman, *New J. Chem.* 2002, **26**, 508.
[87] Du, Aijun and Sanvito, Stefano and Smith, Sean C. *Phys. Rev. Lett.* 2012, **108**, 197207.
[88] Hu Tao and Hashmi Arqum and Hong Jisang. *Sci. Rep.* 2016, **4**, 6059
[89] Hashmi Arqum and Hong Jisang. *Sci. Rep.* 2014, **4**, 4374.
[90] H. Wu, Y. Liu, E. Kan, Y. Ma, W. Xu, J. Li, M. Yan, R. Lu, J. Wei, Y. Qian, *Appl. Phys.* 2016, **49**, 295301.
[91] X. Zhang, M. Zhao, A. Wang, X. Wang, A. Du, *J. Mater. Chem. C* 2013, **1**, 6265.
[92] Q. Hu, Q. Wu, H. Wang, J. He, G. Zhang, *Physica Status Solidi (b)* 2011, **249**, 784.
[93] H. J. Xiang, B. Huang, Z. Y. Li, S.-H. Wei, J. L. Yang, X. G. Gong, *Phys. Rev. X* **2**, 2012, 011003.